Stretched-Coordinate PML in 2D TLM Simulations

Jomiloju S. Odeyemi [1*], Ana Vukovic [1], Trevor M. Benson [1], Phillip Sewell [1]

[1] George Green Institute for Electromagnetics Research, Faculty of Engineering, University of Nottingham, University Park, Nottingham NG7 2RD, UK
[*]Jomiloju.Odeyemi@nottingham.ac.uk.

Abstract: A novel implementation of the stretched coordinate perfectly matched layer (PML) is presented for the two-dimensional (2D) Transmission Line Modelling (TLM) method. The formulation offers a unified approach and is based on the mapping of the TLM node to a complex stretched domain for which the resulting transformation of the constituent RLC transmission line components is elaborated. The transformation is shown to modify the TLM connect-scatter algorithm. The absorption performance is demonstrated by simulating a canonical waveguide test case. Unlike the existing split-field based TLM-PML implementations, which are better suited to lossless media, the numerical results obtained show the proposed PML formulation is effective in the termination of both lossy and lossless media.

1. Introduction

Numerical simulations of open boundary problems require special boundary treatments to be applied on the edges of computational domain in order to accurately simulate the conditions of an infinite propagating medium. The perfectly matched layer (PML) as developed by Bérenger offers a powerful and effective solution to this challenge [1],[2]. Originally devised in the Finite-Difference Time Domain (FDTD) method, the PML is an artificial absorbing layer introduced at the edge of the computational domain which achieves a reflection free outward propagation by an impedance matching scheme. The key attraction of the PML is the theoretically perfect absorption attainable for all angles and frequencies of incidence. Owing to its simplicity and success, various revisions and extensions of Bérenger's original PML proposal have been formulated [2]-[9]. For a given numerical method, there are three approaches which can be employed to implement the PML, namely: the split-field method [1], the anisotropic method [3]-[4] and the stretched coordinate (SC) method [5]. The split field technique involves decomposing each field term into sub-components and applying matched electric and magnetic losses to absorb them along a direction of propagation. This has demonstrated effectiveness in terminating lossless media/free space. However, its application to lossy media creates high reflections at the medium/PML interface. In the anisotropic approach, the PML is implemented as an artificial material possessing uniaxial permeability and permittivity tensors. The SC PML is developed based on imposing an analytical continuation of the fields which maps real to complex coordinates. The complex domain mapping thus transforms the previously propagating fields into exponentially decaying fields. Compared to the split-field interpretation, the anisotropic and SC PMLs offer a simpler implementation which can be easily generalized to non-Cartesian coordinate systems as well as to inhomogeneous and lossy media [4],[10]. The choice of the particular PML approach is strongly influenced by the particular nature of the numerical method in which it is being employed, for example, Finite element, FDTD, transmission line modeling (TLM) method etc.

Critical measures of success for a PML implementation are (i) the effectiveness of the PML in absorbing energy without reflection over a wide range of frequencies, angles of incidence and material properties, (ii) guaranteed algorithmic stability, (iii) ease of incorporation into legacy codes. To date, only a handful of PML formulations have been demonstrated in the TLM method and included in these are three implementations [6]-[8] proposed for two-dimensional (2D) TLM simulations. This is in sharp contrast to the FDTD method, where numerous PML schemes have been deployed some of which are reviewed in [2]. The shortage of TLM-PML implementations is however not an indication of a lack of interest amongst the TLM community. Rather, this is a testament to the challenge presented in implementing an efficient and numerically stable PML in TLM. The first 2D TLM-PML implementation was developed based on a coupling between the TLM-FDTD network [6]. A limitation with this formulation, however, is the non-unified approach taken which introduces parasitic reflections at the TLM-FDTD interface. A unified development was subsequently proposed and implemented for a 2D TLM hybrid node [7] which demonstrated better absorption properties than [6]. Both PML formulations in [6] and [7] have been developed based on Bérenger's original split-field interpretation [1] and are therefore less effective in terminating lossy media. An anisotropic 2D TLM-PML was developed in [8], but was reported unstable and therefore unusable.

In light of the above, this paper develops the framework introduced in our recent work [11] and provides for the first time a comprehensive derivation for implementing the stretched coordinate PML in 2D TLM. The proposed formulation is developed based on an analogy between the equations describing the TLM shunt node and the modified (stretched) second-order wave equations. This process is physically equivalent to mapping the TLM node to a complex stretched space in which the PML region is defined. Unlike the formulations demonstrated in [6]-[8], the mapping of the TLM node reveals a physical transformation of the constitutive RLC transmission line components which make up the transmission network lattice. This provides new insight into the performance of the PML in the TLM method. In contrast to our work in [11], the extensions made in the

present paper reveal the stretching applied on the stubs of the TLM node. This addition enables the formulation to be employed in applications involving inhomogeneous media. This is the advantage over the schemes proposed in [6] and [7]. The framework proposed is simple and can therefore be extended to the implementation of the PML in advanced TLM nodes where such benefits as an improvement in the temporal stabilities have been reported [11].

The rest of the paper is structured as follows. The theory of the mapped shunt node is developed in Section II and the resulting transformation of the transmission line parameters is presented. The modification of the scatter-connect algorithm in the mapped shunt node is derived in Section III. The validity of the method is demonstrated in Section IV as well as its capability for effectively truncating lossy dielectric media. Finally, conclusions from the work are drawn in Section V.

2. Mapping the 2D TLM node to a complex domain

The TLM method bears many similarities with the FDTD method - both are time domain methods and arrive at solutions to wave propagation problems by means of a discretization of time and space [12]-[13]. Unlike FDTD, TLM involves a mapping of Maxwell's equations to transmission line equations and thus translates the fields scattered within a solution space into pulses travelling along equivalent transmission lines in an interconnected network [14].

Based on the physical wave modelling approach employed by TLM, there exists a deep relation between the physical system being modelled and the parameters of a transmission line - such that the geometric and material properties defining the problem space are properly encapsulated into the RLC components of the transmission lines.

Consider the following second-order 2D wave equation for the case where the magnetic field is transverse to the *z* plane (TM_z)

$$\frac{1}{\mu}\frac{\partial^2 E_z}{\partial x^2}+\frac{1}{\mu}\frac{\partial^2 E_z}{\partial y^2}=\epsilon\frac{\partial^2 E_z}{\partial t^2}+\sigma_e\frac{\partial E_z}{\partial t}, \qquad (1)$$

where μ and ϵ are magnetic permeability and electric permittivity, respectively, and σ_e denotes the electrical conductivity. It can be shown [12] that the evolution of the polarized field in a block of three-dimensional (3D) space of dimensions Δl captured by (1) is analogous to the circuit expression

$$\frac{\partial^2 V_z}{\partial x^2}\frac{(\Delta l)^2}{L_t^x}+\frac{\partial^2 V_z}{\partial y^2}\frac{(\Delta l)^2}{L_t^y}=2C_t^z\frac{\partial^2 V_z}{\partial t^2}+G_e\frac{\partial V_z}{\partial t}, \qquad (2)$$

where L_t^x and L_t^y represents the total *x* and *y*-directed node inductance, respectively, and C_t^z and V_z denote the total *z*-directed node capacitance and voltage, respectively, and G_e represents the conductance in the node. A suitable circuit structure, referred to as a "shunt node", which models the behaviour in (2) is illustrated in Fig. 1. Alternatively, the shunt node can be represented as two intersecting transmission lines to make up part of a TLM network in the (*x*-*y*) plane [12].

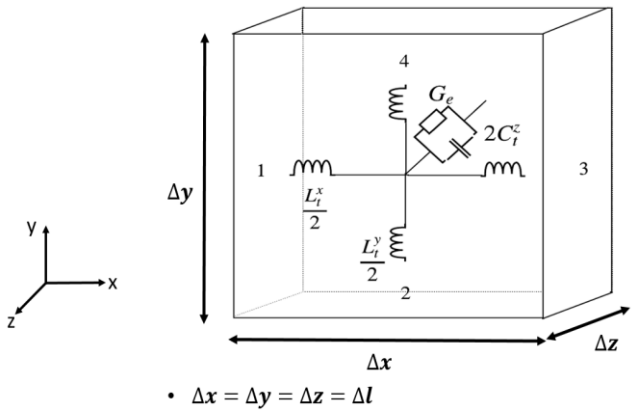

- $\Delta x = \Delta y = \Delta z = \Delta l$

Fig.1. *The TLM shunt node modelling a block of space with dimensions* Δl

By comparing the forms of (1) and (2) an equivalence can be established between the field and circuit parameters given as

$$L_t^x \equiv \mu\Delta l \qquad L_t^y \equiv \mu\Delta l$$

$$2C_t^z \equiv \epsilon\Delta l \qquad G_e \equiv \sigma_e\Delta l\,. \qquad (3)$$

According to the stretched coordinate PML theory [5] an analytic continuation mapping real to complex space is imposed which results in the following spatial transformation

$$\partial x \to \tilde{\partial} x = S_x \partial x$$

$$\partial y \to \tilde{\partial} y = S_y \partial y, \qquad (4)$$

where ∂x, ∂y and ∂z are the differential lengths along each coordinate axis and $\sim$ indicates the complex stretched complements. The complex stretch factor is denoted by S_i and is chosen to be

$$S_i = 1+\frac{\sigma_{si}}{j\omega},$$

$$\sigma_{si} = \frac{\sigma_i}{\epsilon_0}\,, \qquad i = x, y \qquad (5)$$

where σ_{si} represents a positive real variable and $\sigma_i \geq 0$ is a conductivity function used to control the attenuation of the incident fields in a PML.

By substituting the spatial derivatives given in (4) into (1) and multiplying both sides by S_xS_y the wave equation in the coordinate stretched domain is obtained as:

$$\frac{1}{\mu}\frac{S_y}{S_x}\frac{\partial^2 E_z}{\partial x^2}+\frac{1}{\mu}\frac{S_x}{S_y}\frac{\partial^2 E_z}{\partial y^2}=\epsilon S_xS_y\frac{\partial^2 E_z}{\partial t^2}+G_eS_xS_y\frac{\partial E_z}{\partial t}. \qquad (6)$$

Comparing the forms of (2) and (6) enables the spatial transformation given in (4) to be mapped on to circuit parameters in the stretched domain as

$$L_t^x \rightarrow \tilde{L}_t^x = \frac{S_x}{S_y} L_t^x = \frac{S_x}{S_y} \mu \Delta l$$

$$L_t^y \rightarrow \tilde{L}_t^y = \frac{S_y}{S_x} L_t^y = \frac{S_y}{S_x} \mu \Delta l$$

$$C_t^z \rightarrow \tilde{C}_t^z = S_x S_y C_t^z = S_x S_y \epsilon \Delta l$$

$$G_e \rightarrow \tilde{G}_e = S_x S_y G_e = S_x S_y \sigma_e \Delta l. \qquad (7)$$

According to (7), the complex coordinate stretching (4) transforms the standard shunt node defined in real space to a mapped shunt node defined in complex space.

In accordance with the TLM general constitutive relation [15], which separates the total node parameters into contributions from distributed line components, it is clear that with the mapped shunt node each distributed line component undergoes a similar transformation to its associated node parameters.

A crucial point for maximizing the efficacy of the PML is that the coordinate stretching must be applied to the numerical algorithm obtained by discretizing the physics and not to the physics which is then discretized anew as otherwise the unstretched *dispersion error* attributable to the discretization will not be impedance matched by the PML. For this reason, (7) is not manipulated to yield lumped element resistances and conductances, but rather maintained in the form of distributed line parameters.

Therefore, the distributed line inductances in the mapped shunt node are transformed in a similar manner to L_t^x and L_t^y, yielding

$$\tilde{L}_x \Delta l = \frac{S_x}{S_y} L_x \Delta l = \frac{S_x}{S_y} L_t^x$$

$$\tilde{L}_y \Delta l = \frac{S_y}{S_x} L_y \Delta l = \frac{S_y}{S_x} L_t^y, \qquad (8)$$

where $\tilde{L}_x$ and $\tilde{L}_y$ represent the inductance distributed along the *x* and *y*-directed lines in the mapped shunt node.

Likewise, the distributed line capacitances are transformed in a similar way to C_t^z to yield

$$\tilde{C}_x \Delta l = S_x S_y C_x \Delta l$$

$$\tilde{C}_y \Delta l = S_x S_y C_y \Delta l$$

$$\tilde{C}_{oz} = S_x S_y C_{oz}, \qquad (9)$$

where $\tilde{C}_x$ and $\tilde{C}_y$ denote the capacitance distributed along the *x* and *y*-directed lines, respectively, and $\tilde{C}_{oz}$ denotes the stub capacitance.

Following from (8)-(9), the propagation delays experienced by pulses propagating along the *x* and *y*-directed lines of the mapped shunt node are given as

$$\tilde{\Delta} t_x = \Delta l \sqrt{\tilde{L}_x \tilde{C}_x} = \Delta l \sqrt{L_x \frac{S_x}{S_y} S_x S_y C_x} = S_x \Delta t_x$$

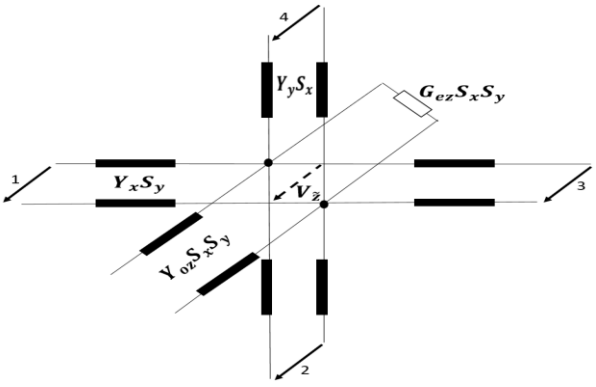

a

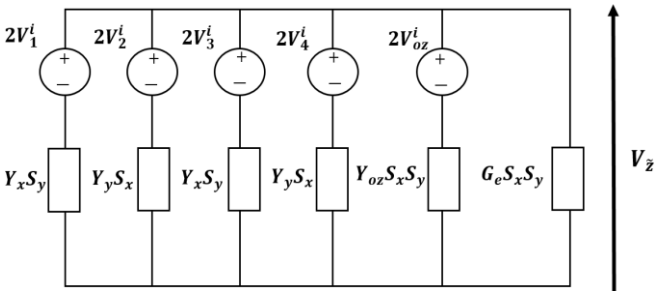

b

Fig. 2. *The mapped shunt node representations.*
(a) TLM equivalent model, **(b)** Thévenin equivalent circuit model

$$\tilde{\Delta} t_y = \Delta l \sqrt{\tilde{L}_y \tilde{C}_y} = \Delta l \sqrt{L_y \frac{S_y}{S_x} S_x S_y C_y} = S_y \Delta t_y,$$

. (10)

where $\tilde{\Delta} t_x$ and $\tilde{\Delta} t_y$ are respectively associated with the *x* and *y*-directed transmission lines.

The resulting characteristic admittance in the mapped shunt node is given as

$$\tilde{Y}_x = \sqrt{\frac{S_x S_y C_x}{\frac{S_x}{S_y} L_x}} = Y_x S_y$$

$$\tilde{Y}_y = \sqrt{\frac{S_x S_y C_y}{\frac{S_y}{S_x} L_y}} = Y_y S_x, \qquad (11)$$

where Y_x and Y_y denote the characteristic admittance along each *x* and *y*-directed transmission line, respectively.

The characteristic admittance of the capacitive stubs Y_{oz} experiences a similar stretching to C_{oz} and is thus given as

$$\tilde{Y}_{oz} = Y_{oz} S_x S_y. \qquad (12)$$

The equivalent circuits representing the mapped shunt node are illustrated in Figs. 2a and b. Both circuits follow the standard form of the shunt node [12] but employ the mapped characteristic admittances. It should also be noted that the

circuit and transmission line parameters of the mapped shunt node reduce to the standard shunt node parameters when $\sigma_i = 0,\ i.e. S_i = 1.$

3. Modified TLM algorithm

The developments made in section II have described how the complex stretching of space in the PML layer transforms the circuit parameters to non-physical components. This section outlines the resulting modifications to the TLM scatter-connect and output processes following the complex domain stretching.

3.1. TLM scatter in the mapped shunt node

In the 2D TLM node, the reflected voltage at each port is given by [12]

$$V_n^r = \tilde{V}_z - V_n^i. \tag{13}$$

where V_n^i is the voltage incident on port *n* and $\tilde{V}_z$ is the total voltage in the mapped shunt node.

Assume that the link line admittances are equal i.e. $Y_x = Y_y = Y_{TL}$, for example, in the case of a free space background medium. By a simple circuit analysis of Fig. 2b the following expression is obtained

$$\tilde{V}_z = 2\frac{S_y(V_1^i + V_3^i) + S_x(V_2^i + V_4^i) + S_xS_y\hat{Y}_{oz}V_{oz}^i}{2S_y + 2S_x + S_xS_y(\hat{G}_{ez} + \hat{Y}_{oz})}, \tag{14}$$

where

$$\hat{Y}_{oz} = \frac{Y_{oz}}{Y_{TL}}, \qquad \hat{G}_{ez} = \frac{G_{ez}}{Y_{TL}}.$$

Arriving at a time domain representation of (14) is nontrivial and requires an appropriate handling of the complex and frequency dependent line admittances. To this end, a series of transformations are deployed for the implementation of digital filters which enable a mapping of frequency dependent material parameters to the time domain and these are [16]:

$$j\omega \rightarrow \quad s \quad \rightarrow \frac{2}{\Delta t}\frac{(1 - z^{-1})}{1 + z^{-1}} \quad \rightarrow \quad [N\Delta t]. \tag{15}$$

where *s* and *z* are the Laplace and Z-transform variables.

Upon a s-domain transformation ($j\omega \rightarrow s$) the stretch factors become $S_x = 1 + \frac{\sigma_{sx}}{s}$, $S_y = 1 + \frac{\sigma_{sy}}{s}$ which, when substituted into (14), yield the expression

$$\tilde{V}_z[s] = \frac{M(s)}{N(s)} \tag{16}$$

where

$$M(s) = 2s(s + \sigma_{sy})(V_1^i + V_3^i) + 2s(s + \sigma_{sx})(V_2^i + V_4^i) + 2(s + \sigma_{sx})(s + \sigma_{sy})\hat{Y}_{oz}$$

and

$$N(s) = s(4s + 2\sigma_{sy} + 2\sigma_{sx}) + (s + \sigma_{sx})(s + \sigma_{sy})(\hat{Y}_{oz} + \hat{G}_{ez}).$$

By applying the bilinear transformation ($s \rightarrow \frac{2}{\Delta t}\frac{1-z^{-1}}{1+z^{-1}}$) to (16) the following Z-transform representation is obtained,

$$\tilde{V}_z[z] = \alpha \begin{bmatrix} Y_{st}\,(V_z - 2V_z z^{-1} + V_z z^{-2}) + \\ \sigma_{sy}\Delta t\left(V_1^i + V_3^i - V_1^i z^{-2} - V_3^i z^{-2}\right) + \\ \sigma_{sx}\Delta t\left(V_2^i + V_4^i - V_2^i z^{-2} - V_4^i z^{-2}\right) + \\ AV_{oz}^i + BV_{oz}^i z^{-1} + CV_{oz}^i z^{-2} + \\ D\tilde{V}_z z^{-1} - E\tilde{V}_z z^{-2} \end{bmatrix} \tag{17}$$

where V_z represents the voltage in the standard shunt node given as

$$V_z = 2\frac{V_1^i + V_2^i + V_3^i + V_4^i + \hat{Y}_{oz}V_{oz}^i}{Y_{st}},$$

and the coefficients are given as

$$Y_{st} = 4 + G$$

$$G = \hat{Y}_{oz} + \hat{G}_{ez}$$

$$A = \hat{Y}_{oz}\left(\sigma_{sx}\Delta t + \sigma_{sy}\Delta t + \frac{\sigma_{sx}\sigma_{sy}\Delta t^2}{2}\right)$$

$$B = \hat{Y}_{oz}\sigma_{sx}\sigma_{sy}\Delta t^2$$

$$C = \hat{Y}_{oz}\left(-\sigma_{sx}\Delta t - \sigma_{sy}\Delta t + \frac{\sigma_{sx}\sigma_{sy}\Delta t^2}{2}\right)$$

$$D = 8 + G\left(2 - \frac{\sigma_{sx}\sigma_{sy}\Delta t^2}{2}\right)$$

$$E = 4 + G - \left(1 + \frac{G}{2}\right)(\sigma_{sx}\Delta t + \sigma_{sy}\Delta t) + \frac{G\sigma_{sx}\sigma_{sy}\Delta t^2}{4}$$

$$\alpha = \frac{1}{4 + G + (1 + \frac{G}{2})(\sigma_{sx}\Delta t + \sigma_{sy}\Delta t) + \frac{G\sigma_{sx}\sigma_{sy}\Delta t^2}{4}}.$$

To obtain a discrete time domain representation of $V_{\tilde{z}}[z]$ an inverse Z-transform is performed on (17) where z^{-p} indicates use of the sample at the previous time step, $(N - p)\Delta t$, denoted as " $_{N-p}$ ". This yields a compact formulation

$${}_N\tilde{V}_z = \alpha_{st}\,{}_NV_z + {}_NV_z^{PML}, \tag{18}$$

where $\alpha_{st} = \alpha Y_{st}$ and the PML voltage ${}_NV_z^{PML}$ represents a digital filter attributed to the analytical continuation given as

$${}_NV_z^{PML} = \alpha \begin{bmatrix} Y_{st}\,({}_{N-2}V_Z - 2\,{}_{N-1}V_Z) + \\ +\sigma_{sy}\Delta t({}_NV_1^i + {}_NV_3^i - {}_{N-2}V_1^i - {}_{N-2}V_3^i) + \\ \sigma_{sx}\Delta t({}_NV_2^i + {}_NV_4^i - {}_{N-2}V_2^i - {}_{N-2}V_4^i) + \\ A\,{}_NV_{oz}^i - B\,{}_{N-1}V_{oz}^i + C\,{}_{N-2}V_{oz}^i + \\ +D\,{}_{N-1}\tilde{V}_z - E\,{}_{N-2}\tilde{V}_z \end{bmatrix}. \tag{19}$$

We note that for the case where $\sigma_{sx} = \sigma_{sy} = 0$ then ${}_N V_z^{PML} = 0$ and $\alpha_{st} = 1$ which reduces ${}_N V_{\tilde{z}}$ to the standard voltage ${}_N V_z$ in the shunt node.

Substituting (18) into (13) yields an expression for the reflected voltage which, for example, at ports 1 and 3 is given as

$$ {}_N V_{1,3}^r = \alpha_{st}\, {}_N V_z - {}_N V_{1,3}^i + {}_N V_z^{PML}. \tag{20} $$

The TLM scatter process for the mapped shunt node can thus be succinctly expressed by the scattering matrix (see (21)).

3.2. TLM connect in the mapped shunt node

Fundamental to the TLM method is its treatment of the incident and reflected voltage-pulses as propagating time impulses [12]-[13]. Following a TLM scatter each reflected voltage impulse $V^r(t)$ becomes the incident impulse on the adjacent transmission line at the next time step. This defines the TLM connect process which is given as

$$ \begin{aligned} V_1^i(x+\Delta x, y, t) &= V_3^r\left(x, y, t-\tilde{\Delta}t_x\right) \\ V_2^i(x, y+\Delta y, t) &= V_4^r\left(x, y, t-\tilde{\Delta}t_y\right) \\ V_3^i(x-\Delta x, y, t) &= V_1^r\left(x, y, t-\tilde{\Delta}t_x\right) \\ V_4^i(x, y-\Delta y, t) &= V_2^r\left(x, y, t-\tilde{\Delta}t_y\right). \end{aligned} \tag{22} $$

The time $\tilde{\Delta}t_i$ delay can be interpreted through a Fourier transform as a phase shift $e^{-j\omega\tilde{\Delta}t_i}$ where $\tilde{\Delta}t_i = \Delta t_i S_i$ which according to (10) is given as $\Delta t_i S_i = \Delta t_i \left(1 + \frac{\sigma_{si}}{j\omega}\right)$ and thus results in

$$ e^{-j\omega\tilde{\Delta}t_i} = e^{-j\omega\Delta t_i} e^{-\Delta t\sigma_{si}}. \tag{23} $$

From (23) it is clear that in the mapped shunt node the time delay is the same as the standard shunt node, however the complex component of $\tilde{\Delta}t_i$ introduces a scaling factor $e^{-\Delta t\sigma_{si}}$ to the reflected pulses propagating along the axis of the coordinate stretching. Therefore, the TLM criterion of impulse synchronism [12]-[13] is maintained, since the real component of Δt_i is unchanged i.e. $\Delta t_x = \Delta t_y = \Delta t$. The full connect equation in the mapped shunt node is therefore given as

$$ \begin{aligned} V_1^i(x+\Delta x, y, t) &= V_3^r(x, y, t-\Delta t)e^{-\Delta t\sigma_{sx}} \\ V_3^i(x-\Delta x, y, t) &= V_1^r(x, y, t-\Delta t)e^{-\Delta t\sigma_{sx}} \\ V_2^i(x, y+\Delta y, t) &= V_4^r(x, y, t-\Delta t)e^{-\Delta t\sigma_{sy}} \\ V_4^i(x, y-\Delta y, t) &= V_2^r(x, y, t-\Delta t)e^{-\Delta t\sigma_{sy}} \end{aligned} $$

$$ V_{oz}^i(x, y, t) = V_{oz}^r(x, y, t-\Delta t). \tag{24} $$

3.3. Output in the mapped shunt node

As with the standard TLM node, the fields are easily obtained at the node centre. The electric and magnetic field components are thus given by [12]

$$ \tilde{E}_z = -\frac{\tilde{V}_z}{\Delta l}. \tag{25} $$

$$ \tilde{H}_y = \frac{\tilde{I}_x}{\Delta l}, \qquad \tilde{H}_x = \frac{\tilde{I}_y}{\Delta l}, \tag{26} $$

where $\tilde{I}_x$ and $\tilde{I}_y$ denote the x and y-directed currents, respectively, in the mapped shunt node. These are given as

$$ \tilde{I}_x = S_y I_x, \qquad \tilde{I}_y = S_x I_y \tag{27} $$

where

$$ I_x = Y_x(V_1^i - V_3^i), \qquad I_y = Y_y(V_4^i - V_2^i). \tag{28} $$

By applying variable transformation (15) to (27) we obtain the following time domain expressions

$$ \begin{aligned} {}_N\tilde{I}_x &= \frac{{}_N I_x\left(2+\sigma_{sy}\Delta t\right) + {}_{N-1}I_x\left(\sigma_{sy}\Delta t - 2\right) + 2\,{}_{N-1}\tilde{I}_x}{2} \\ {}_N\tilde{I}_y &= \frac{{}_N I_y(2+\sigma_{sx}\Delta t) + {}_{N-1}I_y(\sigma_{sx}\Delta t - 2) + 2\,{}_{N-1}\tilde{I}_y}{2}. \end{aligned} \tag{29} $$

4. Numerical experiments

The canonical test case of a wave incident in a $250\Delta l$ (Δl = 0.22 mm) length rectangular waveguide WR28 provides a reliable example to validate the numerical method. The geometry of the simulated waveguide is shown in Fig. 3. As depicted, both ends of the guide were truncated by 25 layers of mapped shunt node PML backed by a perfect electrical conductor (PEC).

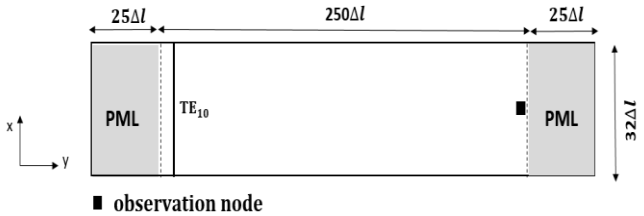

Fig. 3 *Geometry of the rectangular waveguide WR28*

The fundamental TE_{10} mode was excited at one end of the waveguide with a 32.5 GHz sinusoidal amplitude modulated Gaussian pulse of 15 GHz bandwidth**.** The

$$ \begin{bmatrix} {}_N V_1^r \\ {}_N V_2^r \\ {}_N V_3^r \\ {}_N V_4^r \\ {}_N V_{oz}^r \end{bmatrix} = \begin{bmatrix} 2\alpha - 1 & 2\alpha & 2\alpha & 2\alpha & 2\hat{Y}_{oz}\alpha \\ 2\alpha & 2\alpha - 1 & 2\alpha & 2\alpha & 2\hat{Y}_{oz}\alpha \\ 2\alpha & 2\alpha & 2\alpha - 1 & 2\alpha & 2\hat{Y}_{oz}\alpha \\ 2\alpha & 2\alpha & 2\alpha & 2\alpha - 1 & 2\hat{Y}_{oz}\alpha \\ 2\alpha & 2\alpha & 2\alpha & 2\alpha & 2\hat{Y}_{oz}\alpha - 1 \end{bmatrix} \begin{bmatrix} {}_N V_1^i \\ {}_N V_2^i \\ {}_N V_3^i \\ {}_N V_4^i \\ {}_N V_{oz}^i \end{bmatrix} + {}_N V_z^{PML} \tag{21} $$

observation point (shown as a black square in Fig. 3) was positioned at the other end of the guide-one node away from the medium-PML interface. The reflection coefficient was extracted using a reference result obtained by extending the length of the structure such that no energy is incident on the ends over the time period of the simulation. The simulations were operated at the maximum permissible time step $\Delta t = \frac{\Delta l}{c\sqrt{2}}$.

In order to demonstrate the absorption performance of the mapped shunt node PML a comparison was made against the results obtained from waveguides terminated by the TLM-PML formulation presented in [7] and a conventional TLM matched boundary [12] . The maximum conductivity across both PMLs was set at $\sigma_{max} = 10\ S/m$ which was graded across the PML cells using a parabolic profile. As shown in Fig. 4, both PML schemes demonstrate better absorption (>50 dB) compared to the matched boundary termination and better absorption than the non-unified PML reported in [6]. Figure 4 also shows that a comparable level of absorption is achieved by both PML schemes where reflection levels lower than -70 dB are obtained in the mapped shunt node PML over the entire band of operation.

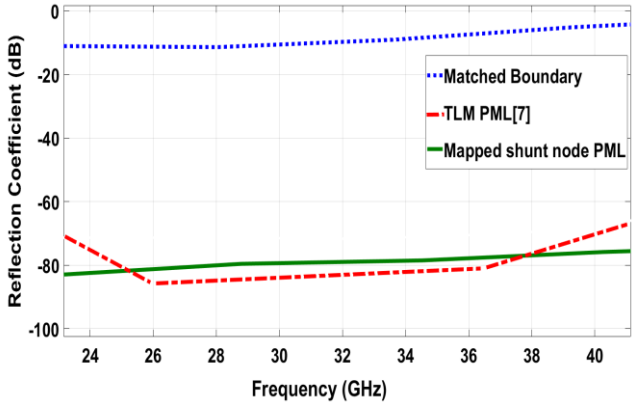

Fig. 4 *Numerical reflection coefficients extracted from a TLM simulation of an empty WR28 rectangular waveguide with various boundary conditions applied*

Subsequently, an investigation on the effect of the transitional reflections arising from the TLM discretization process was carried out. This is of particular interest in this formulation since inter-node reflections are generated due to the mismatch of transmission line impedance across adjacent PML nodes and at the medium-to-layer interface. Figure 5 compares the absorption performance of various conductivity profiles in the above waveguide, namely uniform (n=0), linear (n=1), parabolic (n=2) and cubic (n=3) and for various conductivities. The results presented show that the least absorption is demonstrated by the uniform conductivity profile with a reflection coefficient in the range of -59 dB to -70 dB across the bandwidth of operation. The reflections produced when employing the uniform conductivity profile solely arise at the medium-to-layer interface, and whilst the absorption at the interface can be improved by lowering the conductivity and substantially increasing the PML thickness this results in a significant increase in computational costs. An alternative approach is to use a graded conductivity across the PML. The improvements obtained are reported in Fig. 5 showing that lower reflection levels are achieved compared to the constant profile, n=0, case. The best performing conductivity profile is shown to be the parabolic grading which is in agreement with the findings reported in [1].

The absorption capability of the mapped shunt node PML in a lossy dielectric host was demonstrated by simulating the above waveguide but filled with the following materials: (a) $\epsilon_r = 1, \sigma_e = 0\ S/m$ (freespace); (b) $\epsilon_r = 5, \sigma_e = 0\ S/m$; (c) $\epsilon_r = 1, \sigma_e = 0.5\ S/m$ and (d) $\epsilon_r = 5, \sigma_e = 0.5\ S/m$. The results are presented in Fig. 6 which shows a good absorption performance (>70 dB) is maintained even when incorporating lossy media whilst an increase in the medium's relative permittivity $\epsilon_r > 1$ is shown to reduce the overall absorption.

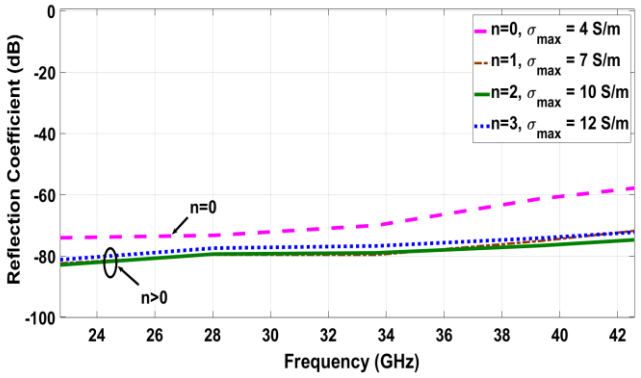

Fig. 5 *Numerical reflection coefficients of the mapped shunt node PML with conductivity profiles: uniform (n=0), linear (n=1), parabolic (n=2), cubic (n=3), as simulated for the waveguide WR28*

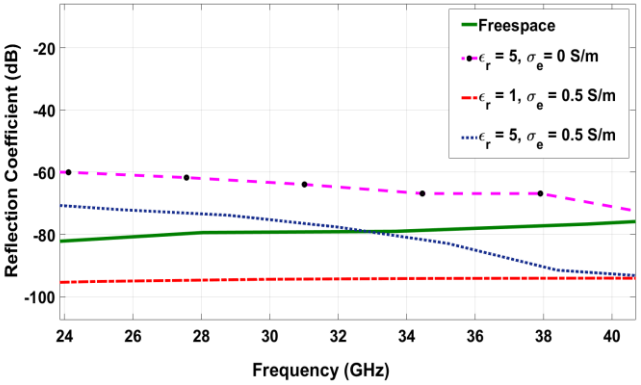

Fig. 6 *Numerical reflection coefficient of the mapped shunt node PML for a WR28 waveguide filled with lossy dielectric media*

For further illustrative purposes the mapped PML is applied to a topical wave-structure application, involving the plane wave scattering of a PEC airfoil with profile Naca0015 [17]. The airfoil structure was placed in a 0.6 m × 2 m computational domain which was uniformly meshed with Δl = 5 mm. The plane wave was incident on the airfoil along the *x* direction. The electric field intensity (in dB) at time t = 30 ns in simulations where a 20 layer PML and matched boundary termination were applied is shown in Figs. 7a and b, respectively. The high absorbing capability of the PML is clearly demonstrated by how quickly the overall energy is attenuated in Fig. 7b compared to Fig. 7a where the matched boundary is employed.

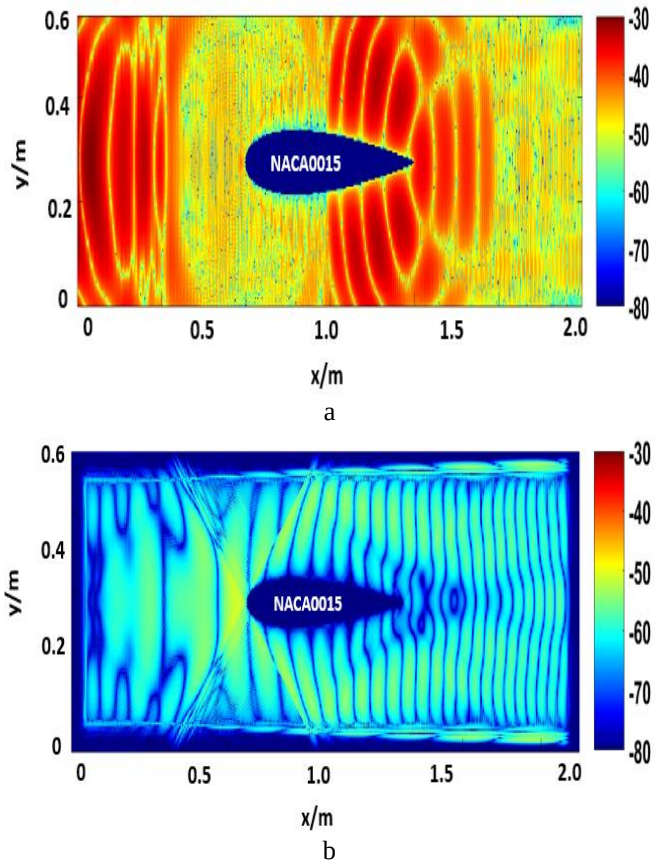

Fig. 7 *Scattered electric field intensity captured at t = 30 ns from a NACA0015 airfoil with*
(a) TLM matched boundary, **(b) 20** layer PML applied at all edges of the domain

Finally, it should be reported that numerical instability has not been observed in any of the investigations carried out in this work; therefore, further demonstrating the utility of the proposed formulation.

5. Conclusion

The PML is widely accepted as the superior absorbing boundary technique and has become a prevalent feature in electromagnetic simulation packages. However, the challenge of developing an efficient and numerically stable TLM-PML formulation is also very well identified amongst TLM researchers. Hence, only a handful of implementations have been reported to date. In light of the huge benefits attainable, we implement, for the first time, a stretched coordinate PML suitable for terminating 2D TLM grids. The method is demonstrated through a mapping of the TLM shunt node to a domain with spatial coordinates stretched to a complex domain. In the proposed formulation, the PML layer is to be interpreted as a network of transmission lines whose constitutive RLC components have been transformed by a complex stretch factor. This formulation offers a unified algorithm and is particularly advantageous as the results obtained show a capability for effectively terminating both lossy and lossless dielectric media. Owing to its simplicity, extensions to other TLM nodes, such as the 2D series node and the widely used three-dimensional symmetrical condensed node, are implicitly implied.

6. References

[1] Bérenger, J.P.:'A perfectly matched layer for the absorption of electromagnetic waves', J. Comput. Phys., 1994, 114, (1), pp. 185–200

[2] Bérenger, J.P.:'Perfectly matched layer (PML) for computational electromagnetics. Synthesis lectures on computational electromagnetics', Morgan and Claypool, 2007

[3] Sacks, Z.S., Kingsland, D.M., Lee, R., Lee, J.F.: 'A perfectly matched anisotropic absorber for use as an absorbing boundary condition', IEEE Trans. Antennas and Propagation, 1995, 43, (12), pp. 1460–1463

[4] Gedney, S.: 'An anisotropic PML for FDTD simulation of fields in lossy dispersive media', Electromagn., 1996,16, (3), pp.339-416

[5] Chew, W.C., Weedon, W.H.: 'A 3D perfectly matched medium from modified Maxwell's equations with stretched coordinates', Microwave and Optical Tech. Lett., 1994, 7, (13), pp. 599–604

[6] Eswarappa, C., Hoefer, W.J.R.: 'Implementation of Bérenger absorbing boundary conditions in TLM by interfacing FDTD perfectly matched layers', Electron. Lett., 1995, 31, (15), pp. 1264-1266

[7] Pena, N., Ney, M.M. 'A new TLM node for Berenger's perfectly matched layer', IEEE Microwave and Guided Wave Lett., 1996, 6, (11), pp. 410-412

[8] Harshana, D.G.: 'Application of TLM for optical microresonators'. PhD thesis, University of Nottingham, 2012

[9] Dubard, J.L., Pompei, D.: 'Optimization of the PML efficiency in 3-D TLM method', IEEE Trans. Microwave Theory and Techniques; 2000, 48(7), pp.1081–1087

[10] Fang, F., Wu, Z.: 'Generalized perfectly matched layer—An extension of Berenger's perfectly matched layer boundary condition', IEEE Microwave Guided Wave Lett., 1995, 5, pp. 451–453

[11] Odeyemi, J.S., Vukovic, A., Benson, T.M., Sewell, P.: 'An Improved PML implementation in the transmission line method', IET 10th Int. Conf. on Computational Electromagnetics, Edinburgh, U.K., June 2019

[12] Christopoulos, C.: 'The transmission-line modeling method: TLM' (Institute of Electrical and Electronics Engineers, New York, 1995)

[13] Hoefer, W.J.R.: 'The transmission-line matrix method—Theory and applications', IEEE Trans. Microwave Theory Tech., 1985, 33, pp. 882-893

[14] Johns, P.B.: 'On the relationship between TLM and finite difference methods for Maxwell's equations', IEEE Trans. Microwave Theory Tech, 1987, 35, pp. 60-61

[15] Trenkic, V., Christopoulos C., Benson, T.M.: 'A unified approach to the derivation of TLM node parameters,' in First International Workshop on TLM, Victoria, Canada, 1995, pp.23-26

[16] Paul. J., Christopoulos. C., Thomas, D.W.P.: ‘Generalized material models in TLM – Part 1: Materials with frequency dependent properties’, IEEE Trans. Antennas and Propagation, 1999, 50, (7), pp. 997-1004

[17] Akbiyik. H., Yavuz. H., Akansu. Y.E., ‘Investigation of the effect of the plasma actuators vertically placed on the spanwise of NACA0015 airfoil,’ in Proc. 8th Int. Exergy, Energy Environ. Symp., 2013, pp. 593–597